

# Topological Time-series Analysis with Delay-variant Embedding

Quoc Hoan Tran\* and Yoshihiko Hasegawa†

Department of Information and Communication Engineering,  
Graduate School of Information Science and Technology,  
The University of Tokyo, Tokyo 113-8656, Japan

(Dated: May 5, 2022)

Identification of qualitative changes in time-series data offers insights into the dynamics behind these data. Such changes can be detected through topological approaches, which first embed these data into a high-dimensional space using a time-delay parameter and subsequently extract topological features describing the shape of the data from the embedded points. However, the essential topological features extracted at a single time-delay value are not sufficient for evaluating qualitative changes, even when well-chosen time-delay values are used. We therefore propose a delay-variant embedding scheme that constructs the extended topological features by regarding the time delay as a variable parameter, rather than as a single fixed value. This method reveals multiple-time-scale patterns in a time series by allowing observation of variations in topological features, with time delay serving as an extra dimension in topological-feature space. We theoretically prove the constructed topological features to be robust under noise perturbation of the time series. Furthermore, we combine these features with the kernel technique in the machine-learning algorithm to classify general time-series data. We demonstrate the effectiveness of this method in the classification of synthetic noisy biological and real electrocardiogram data. Our method outperforms that based on a single time-delay value and, surprisingly, achieves the highest classification accuracy on average among standard time-series analysis techniques.

Time-series data undergo qualitative changes, such as transitions from a quiescent state to oscillatory dynamics through bifurcations. The identification of such changes enables a deep understanding of the underlying dynamics, but this remains a challenging problem when data are subject to noise. In material science, it has been reported that topological features, which indicate the “shape” of the data, can be used to detect qualitative changes, i.e., phase transitions [1, 2] or transitions in morphological and hierarchical structures [3–6]. Since the topology is a qualitative property and is stable under the influence of noise, the topological features of time-series data are expected to reflect qualitative changes in the dynamics. These features are constructed through delay embedding, which maps a time series  $x(t)$  to  $m$ -dimensional points  $[x(t), x(t-\tau), \dots, x(t-(m-1)\tau)]$  on the embedded space, where  $\tau$  is a predefined time-delay parameter and  $m$  is the embedding dimension. The embedded points constitute geometric features such as clusters and loops, and the topological features, which monitor the emergence and vanishment of geometric features, can be used to characterize the dynamics of the system [7, 8]. The time-delay parameter should reflect the local time scale of patterns in the time series [9–12]; this indicates that the embedding with a single time delay does not capture an adequate amount of information if the time series has multiple patterns with different time scales. This defect limits the power of topological features in time-series analysis.

In this Letter, we propose a *delay-variant embedding* method that constructs topological features by taking  $\tau$  as a variable parameter and monitors topological changes in the embedded space over this variable. We theoretically prove the stability of constructed features against

noise and apply these features to classification of several time-series datasets. We demonstrate that our method outperforms that based on a single  $\tau$  in classifying the oscillatory activity of synthetic noisy biological data. Surprisingly, in classifying real electrocardiogram data, our approach demonstrates a higher average accuracy than several standard time-series analysis techniques.

To qualitatively evaluate the characteristics of the time series, we apply topological data analysis [13], which is a computational method used to characterize the topological features of high-dimensional data. We construct a simplicial-complex model [14, 15] from the points in the embedded space and obtain the topological information as the number, position, and size of single- or multi-dimensional clusters and loops. We build a complex over a set of points if the pairwise distances between them are less than or equal to  $2\varepsilon$ , where  $\varepsilon$  is a given non-negative scale parameter. Different  $\varepsilon$  values result in different complexes and different topological information. If  $\varepsilon$  is sufficiently small, no connections are created and the resulting simplicial complex is no different than the original point; if we increase  $\varepsilon$  gradually, the connection between the points appears, and if  $\varepsilon$  becomes excessively large, all points will be connected with each other and will confer no useful information. When we increase parameter  $\varepsilon$  as a sequence  $\varepsilon_1 < \dots < \varepsilon_n$ , we obtain a sequence of embedded simplicial complexes called *filtration*.

We use persistent homology theory [16, 17] to study topological features across filtration. A practical way to visualize the result of persistent homology is through multi-set points in the 2-dimensional *persistence diagram*. In this diagram (denoted as  $\text{PD}_l^{(2)}$ ), each point  $(b, d)$  represents an  $l$ -dimensional hole (i.e., connected components

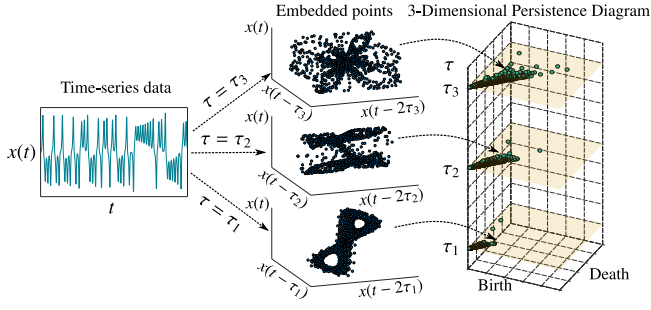


FIG. 1. The time series  $x(t)$  is embedded into an  $m$ -dimensional space (in this illustration,  $m = 3$ ) through delay embedding (left panel). Points in the embedded space at different time delays,  $\tau$ , have different geometric features, such as clusters and loops (middle panel). We extract topological features such as the emergence (birth scale) and vanishment (death scale) of these geometric features. The birth and death scales at each  $\tau$  are represented as points in a 2-dimensional persistence diagram. By observing the variation of topological features with  $\tau$  serving as an extra dimension, we obtain a 3-dimensional persistence diagram (right panel), which can be considered a typical feature of the time series.

are 0-dimensional, loops or tunnels are 1-dimensional holes, and voids are 2-dimensional holes) that appears at  $\varepsilon = b$  (known as the *birth scale*) and disappears at  $\varepsilon = d$  (known as the *death scale*) across the filtration. This information encapsulates the topological features of the time series after embedding and confers valuable insights into the dynamical system's behavior; for instance, the emergence of oscillation in a time series can appear as the birth of a loop in the embedded space. Using these features, the qualitative properties of the time-series data can be captured robustly and efficiently.

For the observed time series  $x(t)$ , we use  $F_{l,\tau}(x(t))$  to denote a 2-dimensional persistence diagram calculated for  $l$ -dimensional holes from embedded points at time delay  $\tau$ . We consider  $\tau$  in a pre-defined set  $\mathcal{T} = \{\tau_1, \tau_2, \dots, \tau_K\}$ , where  $\tau_1 < \tau_2 < \dots < \tau_K$  (with  $K$  denoting the set's size) are sampled from the domain of  $\tau$ . The 3-dimensional persistence diagram for time series  $x(t)$  is defined as  $\text{PD}_l^{(3)}(x(t)) = \{(b, d, \tau) \mid (b, d) \in F_{l,\tau}(x(t)), \tau \in \mathcal{T}\}$ . Figure 1 shows a schematic of the 3-dimensional persistence diagram  $\text{PD}_1^{(3)}(x(t))$  for loops and tunnels (1-dimensional holes), where embedded points show different shapes and topological features at different values of  $\tau$ . In the middle panel of Fig. 1, at  $\tau_1$ , there are two big loops, while at  $\tau_2$  or  $\tau_3$ , loops survive for shorter times, with a different distribution of birth and death scales (right panel). This information cannot be obtained with a single  $\tau$  in the embedding.

Time-series data tend to be very noisy, which may be an artifact of the measurement or be inherent to the dynamics themselves; hence, the diagrams should be stable against perturbation of the data. To evaluate the stability, we introduce the concept of *bottleneck distance* as

a metric structure for comparing diagrams. In a persistence diagram, all points are located in the region where  $b < d$ . Given two 3-dimensional diagrams  $Dg_1^{(3)}$  and  $Dg_2^{(3)}$ , consider all matchings  $\psi$  such that a point on a diagram is matched to a point on the other or to its projection on the diagonal plane  $\mathcal{W}^{(3)} = \{(b, b, \tau) \mid b, \tau \in \mathbb{R}\}$  (Fig. 2(a)). For each pair  $(\mathbf{p}, \mathbf{q}) \in \psi$  for which  $\mathbf{p} = (b_1, d_1, \tau_1)$  and  $\mathbf{q} = (b_2, d_2, \tau_2)$ , we define the *relative infinity-norm distance* between  $\mathbf{p}$  and  $\mathbf{q}$  as  $d_\xi^{(\infty)}(\mathbf{p}, \mathbf{q}) = \max(|b_1 - b_2|, |d_1 - d_2|, \xi|\tau_1 - \tau_2|)$ , where  $\xi$  is a positive rescaling coefficient introduced to adjust the scale difference between the point-wise distance and time. The bottleneck distance,  $d_{B,\xi}^{(3)}(Dg_1^{(3)}, Dg_2^{(3)})$ , is defined as the infimum of the longest matched relative infinity-norm distance over all matchings,  $\psi$ :

$$d_{B,\xi}^{(3)}(Dg_1^{(3)}, Dg_2^{(3)}) = \inf_{\psi} \max_{(\mathbf{p}, \mathbf{q}) \in \psi} d_\xi^{(\infty)}(\mathbf{p}, \mathbf{q}). \quad (1)$$

We show that 3-dimensional persistence diagrams are stable with respect to the bottleneck distance under perturbation applied to the time series. Given two time series,  $x(t)$  and  $y(t)$ , with the same length, let  $Dg_{(m)}^{(3)}(x)$  and  $Dg_{(m)}^{(3)}(y)$  be 3-dimensional persistence diagrams for each respective series, as calculated at the embedding dimension  $m$ . Inspired by the stability properties of 2-dimensional persistence diagrams [18], in [15], we prove the following stability property of the 3-dimensional ones:

$$d_{B,\xi}^{(3)}(Dg_{(m)}^{(3)}(x), Dg_{(m)}^{(3)}(y)) \leq 2\sqrt{m} \max_t |x(t) - y(t)|, \quad (2)$$

for arbitrary positive rescaling coefficient  $\xi$ . When we identify  $y(t)$  as the perturbed data obtained by adding noise to  $x(t)$ , Eq. (2) shows that the bottleneck distance between  $Dg_{(m)}^{(3)}(x)$  and  $Dg_{(m)}^{(3)}(y)$  is bounded from above by the noise's magnitude.

To use persistence diagrams as features for statistical-learning tasks such as classification, we need to define a similarity measure such as a kernel mapping for such diagrams [2, 19, 20]. Since the points close to  $\mathcal{W}^{(3)}$  can be neglected as insignificant topological features, they should not influence the computed value of this kernel. Given a positive bandwidth  $\sigma$  and the positive rescaling parameter  $\xi$ , we define the kernel  $k_{\sigma,\xi}$  between two 3-dimensional persistence diagrams,  $Dg_1^{(3)}$  and  $Dg_2^{(3)}$ , as  $k_{\sigma,\xi}(Dg_1^{(3)}, Dg_2^{(3)}) = \frac{1}{\sigma\sqrt{2\pi}} \sum_{\mathbf{p} \in Dg_1^{(3)}, \mathbf{q} \in Dg_2^{(3)}} \left( e^{-\frac{d_\xi^2(\mathbf{p}, \mathbf{q})}{2\sigma^2}} - e^{-\frac{d_\xi^2(\mathbf{p}, \bar{\mathbf{q}})}{2\sigma^2}} \right)$ , where  $\bar{\mathbf{q}}$  is a symmetric point of  $\mathbf{q}$  with respect to  $\mathcal{W}^{(3)}$  and  $d_\xi^2(\mathbf{p}, \mathbf{q}) = |b_1 - b_2|^2 + |d_1 - d_2|^2 + \xi^2|\tau_1 - \tau_2|^2$ ,  $d_\xi^2(\mathbf{p}, \bar{\mathbf{q}}) = |b_1 - d_2|^2 + |d_1 - b_2|^2 + \xi^2|\tau_1 - \tau_2|^2$ , with  $\mathbf{p} = (b_1, d_1, \tau_1)$  and  $\mathbf{q} = (b_2, d_2, \tau_2)$ . If  $\mathbf{p}$  or  $\mathbf{q}$  is near  $\mathcal{W}^{(3)}$ , i.e.,  $b_1 \approx d_1$  or  $b_2 \approx d_2$ , then  $d_\xi^2(\mathbf{p}, \mathbf{q}) \approx d_\xi^2(\mathbf{p}, \bar{\mathbf{q}})$  and the pair  $(\mathbf{p}, \mathbf{q})$  has a smaller influence upon the value of the kernel (Fig. 2(b)). Based on Ref. [19], we can prove that  $k_{\sigma,\xi}$  is a positive-

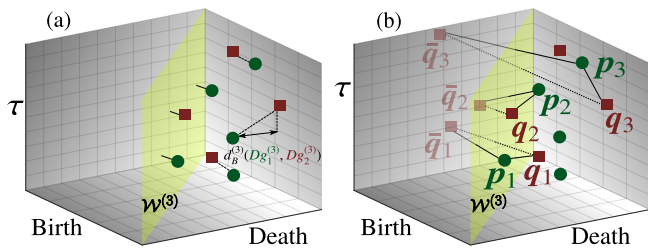


FIG. 2. (a) Bottleneck distance between two diagrams  $Dg_1^{(3)}$  (green points) and  $Dg_2^{(3)}$  (red points). The  $\tau$  axis is rescaled with the positive coefficient  $\xi$  to adjust the scale difference between the point-wise distance and time. A green (red) point is matched to a red (green) point, or to its projection on the diagonal plane,  $\mathcal{W}^{(3)}$ . The distance between two matched points is the longest edge of their differences along any coordinate dimension. The bottleneck distance is defined as the longest distance between two matched points that is minimal compared to all other matchings. (b) Kernel between  $Dg_1^{(3)}$  (green points) and  $Dg_2^{(3)}$  (dark red points). The faint red points are symmetric to the dark red points with respect to  $\mathcal{W}^{(3)}$ . Points near  $\mathcal{W}^{(3)}$ , i.e.,  $p_1, q_2$ , have less influence, whereas the pairs of points far away from  $\mathcal{W}^{(3)}$ , i.e.,  $(p_2, q_1), (p_2, q_3), (p_3, q_1), (p_3, q_3)$ , make essential contributions to the kernel.

definite kernel [15]. When we apply  $k_{\sigma, \xi}$  to the classification of time series, the parameters  $\sigma$  and  $\xi$  affect the classification performance and can be chosen by cross-validation or by a heuristic method [15, 21].

First, we apply the proposed method to classify the periodic and aperiodic time series from synthetic single-cell data. This is challenging due to the difficulty with discriminating noisy oscillation from mere noisy fluctuation [22]. We generate synthetic mRNA and protein time-series data from a stochastic model of the *Hes1* genetic oscillator [23, 24] consisting of negative auto-regulation with delay. We use the delayed version of the Gillespie algorithm [25, 26] to generate data from 1,000 cells in both the oscillatory and non-oscillatory parameter regimes [24, 27]. The protein levels are measured every  $\nu$  ( $\nu = 32, 16, 8$ ) min for 4,096 minutes. We normalize the time series to have a mean of zero and unit variance, then add noise with a variance of 10% of the signal at each time point to show the robustness of the method. In the delay-variant method, we take  $K = 10$  time-delay values as  $\tau_1 = 1, \tau_2 = 2, \dots, \tau_{10} = 10$ . In the single-delay approach,  $\tau$  is selected by the mutual-information method [9]. Figure 3 shows examples of time series and persistence diagrams for the two regimes at an embedding dimension of  $m = 3$ . Figures 3(a) and (d) show the time series generated from (a) non-oscillatory and (d) oscillatory regimes measured every  $\nu = 16$  min. Figures 3(b) and (e) show the 2-dimensional persistence diagrams computed from the single-delay embedding of the time series from Figs. 3(a) and (d), respectively. Figures 3(c) and (f) show 3-dimensional persistence dia-

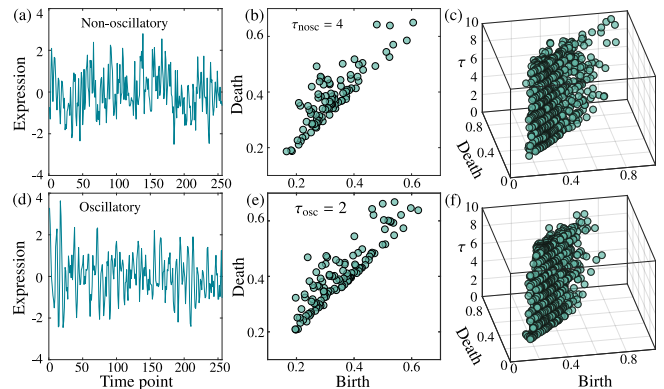


FIG. 3. (a)(d) Examples of two time series generated from (a) the non-oscillatory and (d) oscillatory regimes of the *Hes1* model measured every 16 minutes. (b)(e) 2-dimensional persistence diagrams of loop patterns calculated with an embedding dimension  $m = 3$  and a single  $\tau$  which is selected according to [9] for (b) non-oscillatory ( $\tau = 4$ ) and (e) oscillatory ( $\tau = 2$ ) time series. (c)(f) 3-dimensional persistence diagrams of loop patterns calculated with  $m = 3$  and 10 values of  $\tau$  given by  $\tau_1 = 1, \tau_2 = 2, \dots, \tau_{10} = 10$  for (c) non-oscillatory and (f) oscillatory time series.

grams from Figs. 3(a) and (d), respectively. In these examples, it is difficult to distinguish between two regimes using the original time series or 2-dimensional diagrams, whereas there is a distinct pattern for 3-dimensional diagrams, because all topological variations are considered when  $\tau$  changes.

When using the same embedding dimension  $m$ , the total dimension for the delay-variant method ( $mK$ ) is higher than that for the single-delay method ( $m$ ). In the classification task, higher dimensional features tend to confer higher classification accuracies. Therefore, to make a fair comparison, we define the effective embedding dimension as  $M = mK$ . We validate the effectiveness of the proposed topological features by performing classification of *Hes1*-model data. These data are randomly split 50%-50% into training-test sets. We apply the support vector machine [28] for classification in the kernel space. Figure 4 shows the average classification accuracy over 100 random splits at different effective embedding dimensions  $M$  and different measurement intervals  $\nu$ . Figure 4 demonstrates that the delay-variant method performs significantly better than the single-delay method at  $M \geq 30$ . The accuracy of the delay-variant method does not change over a wide range of  $M$  (from 40 to 100), indicating that this method is reliable. The inset of Fig. 4 represents the maximum accuracy of both methods over the effective embedding dimensions in each  $\nu$ . When  $\nu$  increases, the length of the time series shortens, making classification more difficult; nevertheless, the delay-variant method attains a higher maximum accuracy than the single-delay method. Although the difference in maximum accuracy is about

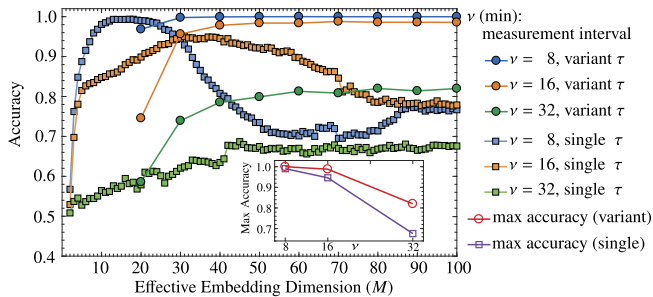


FIG. 4. Average classification accuracy of delay-variant (circle) and single-delay (square) methods over 100 random splits of Hes1-model data at different effective embedding dimensions  $M$  and measurement intervals  $\nu = 8\text{min}$  (blue),  $16\text{min}$  (orange), and  $32\text{min}$  (green). The inset highlights the maximum accuracy of the delay-variant (red circle) and single-delay (purple square) methods over the effective embedding dimensions at each  $\nu$ .

1% for  $\nu = 8\text{min}$  (1.0 (delay-variant) and 0.99 (single-delay)), this difference is significant in terms of the error rate defined by  $(1.0 - \text{accuracy})$ .

We now evaluate the performance of delay-variant method in classifying different heartbeat-signal patterns from six real electrocardiogram datasets (ECG200, ECG5000, ECGFiveDays, TwoLeadECG, Non-InvasiveFetalECGThorax1, Non-InvasiveFetalECGThorax2) with a train-test split provided in [29]. In the single-delay method,  $\tau$  is selected by the mutual-information method [9]. In the delay-variant method, we use  $K = 10$  time-delay values as  $\tau_1 = 1, \tau_2 = 2, \dots, \tau_{10} = 10$ . In both methods, we use a linear combination of kernels at the 0-dimensional and 1-dimensional holes [15]. The weights of the combination and the embedding dimension,  $m$ , are selected by cross-validation. We compare the delay-variant and single-delay methods, as well as some alternative standard approaches. The majority of the research on time-series classification problems has focused on finding appropriate similarity measures for the 1<sup>st</sup>-nearest neighbor (NN) classifier. For similarity in the time domain, we consider the Euclidean (E) or dynamic time wrapping (D) distances. For similarity in the frequency domain or for auto-correlation, we consider the power spectrum (PS) and the auto-correlation function (AC). We also examine the elastic ensemble (EE) [30] as a combination of nearest neighbor classifiers using multiple distance measures in the time domain. Finally, we compare with learned-shapelets (LS) method in [31], which classifies time series by learning the representative *shapelets* (i.e., short discriminant time-series subsequences). Rather than implementing these algorithms, we adopt the results from [32, 33]. The test results are presented in Table I, wherein the best and second-best accuracy scores of each dataset are colored in dark pink and light pink, respectively. The delay-variant method

TABLE I. Classification accuracy (%) with respect to datasets ECG200, ECG5000, ECGFiveDays (FiveDays), TwoLeadECG (TwoLead), Non-InvasiveFetalECGThorax1 (Thorax1), and Non-InvasiveFetalECGThorax2 (Thorax2). In each dataset, the best and second-best scores are colored in dark pink and light pink, respectively. The 1<sup>st</sup>-nearest neighbor classifier is abbreviated NN; Euclidean distance is E, dynamic time wrapping distance is D, auto-correlation function is AC, power spectrum is PS, elastic ensemble is EE, and the learned-shapelets method is LS.

Data	Delay variant	Single delay	NN (E)	NN (D)	NN (AC)	NN (PS)	EE	LS
ECG200	92.0	78.0	88.0	88.0	82.0	86.0	88.0	88.0
ECG5000	93.6	90.4	92.5	92.5	91.0	93.6	93.9	93.2
FiveDays	99.8	72.7	79.7	79.7	98.1	100.0	82.0	100.0
TwoLead	99.3	80.9	74.7	86.8	80.4	96.1	97.1	99.6
Thorax1	91.7	64.2	82.9	82.9	72.1	87.5	84.6	25.9
Thorax2	93.0	70.9	88.0	87.0	75.2	88.4	91.4	77.0

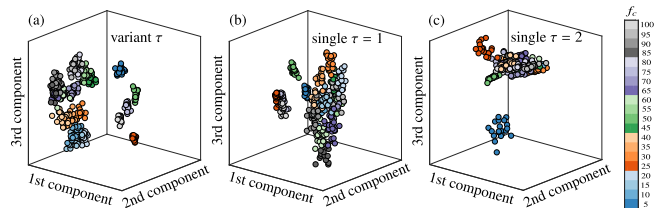


FIG. 5. The projection of features for synthetic frequency modulated time series from the kernel space to the principal components for (a) delay-variant and (b)(c) single-delay at effective embedding dimension  $M = 120$  and  $\tau = 1, 2$ , respectively. Different colors represent data generated from different values of the carrier frequency,  $f_c$ .

shows better results than the single-delay method for all datasets and outperforms all other algorithms on average. For three of the six datasets, it offers the best results, and offers the second-best for three more; this result suggests that our method can be considered to be an effective approach for classifying time series.

We next investigate what kinds of features in the time-series data are effectively captured by the delay-variant method. Because the time delay is related to the time scale of the patterns, it is expected that the delay-variant method should be able to extract patterns consisting of multiple different time scales. To better understand this ability, we analyze the synthetic noisy time series of a frequency-modulated model. Given the original signal  $s_m(t) = A_m \sin(2\pi f_m t)$  with a carrier signal  $s_c(t) = A_c \sin(2\pi f_c t)$  we consider the modulated signal to be  $s(t) = A_c \sin(2\pi f_c t + A_m \sin(2\pi f_m t))$ , where  $t \in [0, 0.1]$  and  $A_m = 10, A_c = 1.0, f_m = 25$ . The frequency  $f_c$  represents multiple-time-scale patterns in the modulated signal. We consider different values of  $f_c$  as  $f_c = 5f$  with  $f = 1-20$ . At each value of  $f_c$ , we generate 20 noisy discrete time series  $z_l(n) = s(0.0002n) + w_l(n)$ , where  $l = 1, 2, \dots, 20, n = 0, 1, \dots, 500$ , and  $w_l(n)$  is the



Gaussian white noise with a variance equal to 0.1. In the delay-variant method, we use  $K = 20$  time-delay values as  $\tau_1 = 1, \tau_2 = 2, \dots, \tau_{20} = 20$ . An example of the principal-components projection from the kernel space is shown in Fig. 5 for the (a) delay-variant and (b)(c) single-delay at effective embedding dimension of  $M = 120$ . As the length of the time series is 501, in the single-delay approach, at  $M = 120$ ,  $\tau$  can only take values from  $\{1, 2, 3, 4\}$ . In Fig. 5(b)(c) we consider  $\tau = 1, 2$ , respectively (see [15] for the result with other values of  $\tau$  and  $M$ ). Different colors represent data generated from different values of  $f_c$ . Figure 5 demonstrates that the delay-variant method shows more distinct regions corresponding to different values of  $f_c$  than the single-delay method. Note that the points in the single-delay method cannot be distinct, regardless of the angle. This result reveals that the delay-variant embedding is superior to the single-delay embedding in terms of discriminating changes in multiple-time-scale patterns in the time series.

We have demonstrated that the topological features constructed from delay-variant embedding can capture topological variants of the time series when the time-delay value changes. The proposed theory guarantees the stability of the features under perturbation of the data. Our method outperformed standard methods in the classification of time series; it can be used to reveal the representative topological features of time series and opens up many possibilities for using topological tools in time-series data analysis.

---

\* [zoro@biom.t.u-tokyo.ac.jp](mailto:zoro@biom.t.u-tokyo.ac.jp)

† [hasegawa@biom.t.u-tokyo.ac.jp](mailto:hasegawa@biom.t.u-tokyo.ac.jp)

- [1] I. Donato, M. Gori, M. Pettini, G. Petri, S. De Nigris, R. Franzosi, and F. Vaccarino, *Phys. Rev. E* **93**, 052138 (2016).
- [2] G. Kusano, K. Fukumizu, and Y. Hiraoka, in *Proc. 33th Int. Conf. Machine Learning (ICML)*, Vol. 48 (2016).
- [3] S. Ardanza-Trevijano, I. Zuriguel, R. Arévalo, and D. Maza, *Phys. Rev. E* **89**, 052212 (2014).
- [4] T. Nakamura, Y. Hiraoka, A. Hirata, E. G. Escolar, and Y. Nishiura, *Nanotechnology* **26**, 304001 (2015).
- [5] Y. Hiraoka, T. Nakamura, A. Hirata, E. G. Escolar, K. Matsue, and Y. Nishiura, *Proc. Natl. Acad. Sci. U.S.A.* **113**, 7035 (2016).
- [6] T. Ichinomiya, I. Obayashi, and Y. Hiraoka, *Phys. Rev. E* **95**, 012504 (2017).
- [7] S. Maletić, Y. Zhao, and M. Rajković, *Chaos* **26**, 053105 (2016).
- [8] K. Mittal and S. Gupta, *Chaos* **27**, 051102 (2017).
- [9] A. M. Fraser and H. L. Swinney, *Phys. Rev. A* **33**, 1134 (1986).
- [10] W. Liebert, K. Pawelzik, and H. G. Schuster, *EPL* **14**, 521 (1991).
- [11] S. P. Garcia and J. S. Almeida, *Phys. Rev. E* **71**, 037204 (2005).
- [12] C. Letellier, I. M. Moroz, and R. Gilmore, *Phys. Rev. E* **78**, 026203 (2008).
- [13] G. Carlsson, *Bull. Amer. Math. Soc.* **46**, 255 (2009).
- [14] H. Edelsbrunner and J. Harer, *Computational Topology. An Introduction*. (Amer. Math. Soc., 2010).
- [15] See Supplemental Material.
- [16] H. Edelsbrunner, D. Letscher, and A. Zomorodian, *Discrete Comput. Geom.* **28**, 511 (2002).
- [17] A. Zomorodian and G. Carlsson, *Discrete Comput. Geom.* **33**, 249 (2005).
- [18] F. Chazal, V. de Silva, and S. Oudot, *Geom. Dedicata* **173**, 193 (2014).
- [19] J. Reininghaus, S. Huber, U. Bauer, and R. Kwitt, in *2015 IEEE Conf. Computer Vision and Pattern Recognition (CVPR)* (2015).
- [20] M. Carrière, M. Cuturi, and S. Oudot, in *Proc. 34th Int. Conf. Machine Learning (ICML)*, Vol. 70 (2017).
- [21] A. Gretton, K. Fukumizu, C. H. Teo, L. Song, B. Schölkopf, and A. J. Smola, in *Advances in Neural Information Processing Systems 20* (2008).
- [22] N. E. Phillips, C. Manning, N. Papalopulu, and M. Rattray, *PLOS Comp. Biol.* **13**, 1 (2017).
- [23] N. A. Monk, *Curr. Biol.* **13**, 1409 (2003).
- [24] T. Galla, *Phys. Rev. E* **80**, 021909 (2009).
- [25] D. T. Gillespie, *J. Phys. Chem.* **81**, 2340 (1977).
- [26] D. F. Anderson, *J. Phys. Chem.* **127**, 214107 (2007).
- [27] T. Brett and T. Galla, *Phys. Rev. Lett.* **110**, 250601 (2013).
- [28] C. M. Bishop, *Pattern Recognition and Machine Learning* (Springer, 2006).
- [29] Y. Chen, E. Keogh, B. Hu, N. Begum, A. Bagnall, A. Mueen, and G. Batista, “The UCR Time Series Classification Archive,” (2015), [www.cs.ucr.edu/~eamonn/time\\_series\\_data/](http://www.cs.ucr.edu/~eamonn/time_series_data/).
- [30] J. Lines and A. Bagnall, *Data Min. Knowl. Disc.* **29**, 565 (2014).
- [31] J. Grabocka, N. Schilling, M. Wistuba, and L. Schmidt-Thieme, in *Proc. 20th ACM SIGKDD Int. Conf. Knowledge Discovery and Data Mining* (2014).
- [32] A. Bagnall, J. Lines, A. Bostrom, J. Large, and E. Keogh, *Data Min. Knowl. Disc.* **31**, 606 (2016).
- [33] A. Bagnall, J. Lines, W. Vickers, and E. Keogh, “The UEA & UCR Time Series Classification Repository,” [www.timeseriesclassification.com](http://www.timeseriesclassification.com).

# Supplemental Material for “Topological Time-series Analysis with Delay-variant Embedding”

Quoc Hoan Tran and Yoshihiko Hasegawa

This supplementary material describes in detail the calculations introduced in the main text. Equation and figure numbers in this section are prefixed with S (e.g., Eq. (S1) or Fig. S1). Numbers without the prefix (e.g., Eq. (1) or Fig. 1) refer to items in the main text.

## 1 Topological features from data

We consider the input data as a set  $P$  of points in the Euclidean space  $\mathbb{R}^L$ . Our main interest is finding the essential topological features, which are considered to be the “shape” of the data. In the main text, topological features are defined as the emergence and vanishment of geometric features such as clusters and loops when considering a sequence of simplicial complexes constructed from points. Here, a simplicial complex is a finite set of simplices where an  $n$ -simplex ( $n = 0, 1, 2, \dots$ ) is a fully connected set of  $n + 1$  affinely independent points.

To extract the topological features from  $P$ , we build a  $\varepsilon$ -scale Vietoris–Rips complex (denoted as  $\text{VR}(P, \varepsilon)$ ) from a union of  $L$ -dimensional hyperspheres of radius  $\varepsilon$  centered at each point in  $P$ . Every collection of  $n + 1$  affinely independent points in  $P$  forms an  $n$ -simplex in  $\text{VR}(P, \varepsilon)$  if the pairwise distance between points is less than or equal to  $2\varepsilon$ . The complex  $\text{VR}(P, \varepsilon)$  gives us the topological information from  $P$  associated with radius  $\varepsilon$ . For example, in Fig. S1(d), there are two loops (called 1-dimensional holes) and one connected component (called a 0-dimensional hole). However, this information depends on how to choose the radius  $\varepsilon$ . If  $\varepsilon$  is too small, the complex created by union hyperspheres (Fig. S1(b)) remains almost the same as the discrete points (Fig. S1(a)). If  $\varepsilon$  is too large, we obtain a trivially connected and overlapped complex without any hole inside it (Fig. S1(f)).

The problem above can be solved by considering not only a single radius, but all choices of radius  $\varepsilon$ . This yields a *filtration*, which is a sequence of simplicial complexes used to monitor the appearance of holes such as clusters and loops over changing  $\varepsilon$ . For example, in Fig. S1, we start from  $\varepsilon = 0$  (Fig. S1(a)); then we increase  $\varepsilon$  gradually to see whether the holes appear or disappear at different values of  $\varepsilon$ . When a hole appears and disappears at radii  $\varepsilon = b$  and  $\varepsilon = d$ , respectively, the hole is characterized by a pair  $(b, d)$ , where  $b$ ,  $d$ , and  $(b, d)$  are referred to as the *birth scale*, *death scale*, and *persistence pair*, respectively. This persistence pair is calculated for all holes that appear in a filtration.

The persistence pairs, which we use as topological features, are displayed in the Cartesian plane as a 2-dimensional persistence diagram where the birth and death scales appear as the horizontal and vertical coordinates, respectively. In the 2-dimensional persistence diagram, points far from the diagonal generally correspond to robust features, which are persistent over a long time, whereas those near the diagonal are regarded as noise in the data. We provide an exemplary 2-dimensional persistence diagram in Fig. S2, where we consider the appearance and disappearance of loops in a filtration of the Vietoris–Rips complex constructed from points when  $\varepsilon$  takes the discrete values from the set  $\{0, 0.1, 0.2, 0.3, 0.4, 0.5, 0.6\}$ . In Fig. S2, there are two persistence pairs  $(0.2, 0.4)$  (blue circle) and  $(0.3, 0.6)$  (red triangle) which represent the appearance and disappearance of a blue loop (appears at  $\varepsilon = 0.2$  then disappears at  $\varepsilon = 0.4$ ) and a red loop (appears at  $\varepsilon = 0.3$  then disappears at  $\varepsilon = 0.6$ ) in the filtration, respectively. Please refer to [1] for more details concerning mathematical definitions and computational algorithms.

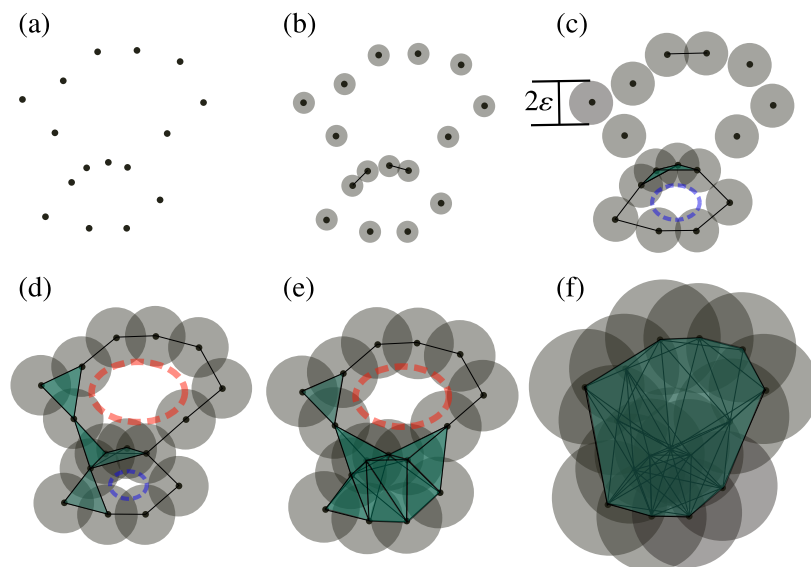


Figure S1: We consider  $L$ -dimensional hyperspheres with radius  $\varepsilon$  centered at each point. From (a) to (f), we increase the radius  $\varepsilon$  gradually. By increasing  $\varepsilon$ , holes appear and disappear in the region. The first 1-dimensional hole (blue loop) appears at (c), while the second (red loop) appears at (d). Then at (e), the first hole disappears and finally the second one disappears at (f).

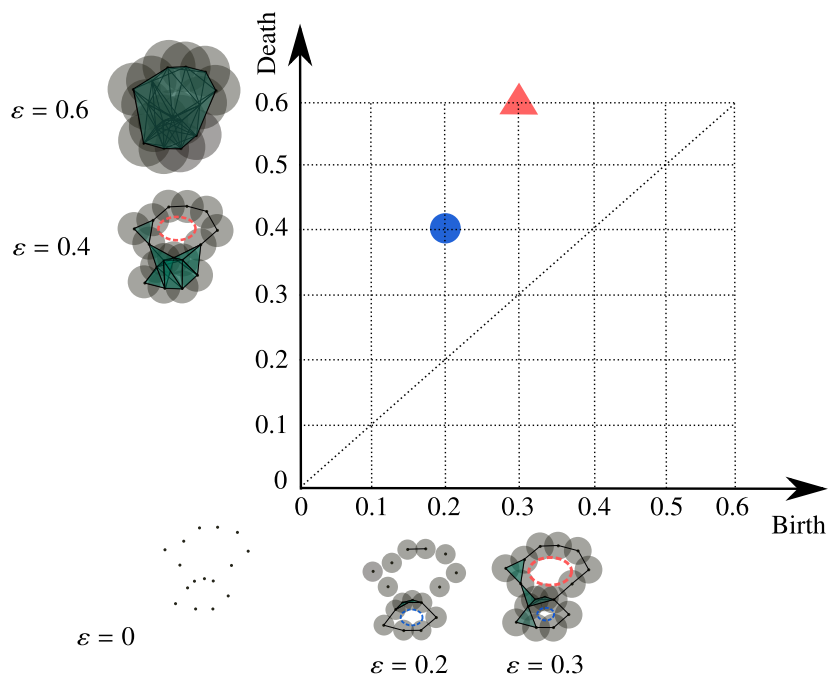


Figure S2: An exemplary 2-dimensional persistence diagram calculated by considering the appearance and disappearance of loops from a filtration of the Vietoris–Rips complex. The radius  $\varepsilon$  takes the discrete values from the set  $\{0, 0.1, 0.2, 0.3, 0.4, 0.5, 0.6\}$ . There are two persistence pairs  $(0.2, 0.4)$  and  $(0.3, 0.6)$ , which represent the appearance and disappearance of the blue loop and the red loop, respectively, in the filtration. These persistence pairs are displayed as a blue circle and a red triangle in the Cartesian plane, respectively. The collection of all the persistence pairs in the filtration is a 2-dimensional persistence diagram.

## 2 Proof of the stability of the 3-dimensional persistence diagram

In the following definitions, the distance  $\|\mathbf{z}\|_\infty$  is defined as  $\max\{|z_1|, \dots, |z_n|\}$  for  $\mathbf{z} = (z_1, \dots, z_n) \in \mathbb{R}^n$ .

First, we introduce the concept of *bottleneck distance* between two 2-dimensional diagrams. Given two 2-dimensional diagrams  $Dg_1^{(2)}$  and  $Dg_2^{(2)}$ , consider all matchings  $\gamma$  such that a point on a diagram is matched to a point on the other or to its projection on the diagonal line  $\mathcal{W}^{(2)} = \{(b, b) \mid b \in \mathbb{R}\}$ . The bottleneck distance  $d_B^{(2)}$  between  $Dg_1^{(2)}$  and  $Dg_2^{(2)}$  is defined as the infimum of the longest matched infinity-norm distance over all matchings,  $\gamma$ :

$$d_B^{(2)}(Dg_1^{(2)}, Dg_2^{(2)}) = \inf_{\gamma} \max_{(\mathbf{p}, \mathbf{q}) \in \gamma} \|\mathbf{p} - \mathbf{q}\|_\infty. \quad (\text{S1})$$

The bottleneck distance between the 2-dimensional persistence diagrams satisfies the following stability property [2]:

**Proposition S1** *Let  $X$  and  $Y$  be finite sets of points embedded in the Euclidean space  $\mathbb{R}^n$ . Denote their 2-dimensional persistent diagrams as  $Dg^{(2)}(X)$  and  $Dg^{(2)}(Y)$ , respectively. Then,*

$$d_B^{(2)}(Dg^{(2)}(X), Dg^{(2)}(Y)) \leq 2d_H(X, Y), \quad (\text{S2})$$

where  $d_H(X, Y)$  is the Hausdorff distance given by

$$d_H(X, Y) = \max \left\{ \max_{\mathbf{x} \in X} \min_{\mathbf{y} \in Y} d(\mathbf{x}, \mathbf{y}), \max_{\mathbf{y} \in Y} \min_{\mathbf{x} \in X} d(\mathbf{x}, \mathbf{y}) \right\}, \quad (\text{S3})$$

where  $d(\mathbf{x}, \mathbf{y})$  is the Euclidean distance between two points  $\mathbf{x}, \mathbf{y}$  in  $\mathbb{R}^n$ .

Next, we define the bottleneck distance for the proposed 3-dimensional persistence diagrams. Given two 3-dimensional diagrams  $Dg_1^{(3)}$  and  $Dg_2^{(3)}$ , consider all matchings  $\psi$  for which a point on a diagram is matched to a point on the other or to its projection on the diagonal plane  $\mathcal{W}^{(3)} = \{(b, b, \tau) \mid b, \tau \in \mathbb{R}\}$ . For each pair  $(\mathbf{p}, \mathbf{q}) \in \psi$  where  $\mathbf{p} = (b_1, d_1, \tau_1)$  and  $\mathbf{q} = (b_2, d_2, \tau_2)$ , we define the *relative infinity-norm distance* between  $\mathbf{p}$  and  $\mathbf{q}$  as  $d_\xi^{(\infty)}(\mathbf{p}, \mathbf{q}) = \max(|b_1 - b_2|, |d_1 - d_2|, \xi|\tau_1 - \tau_2|)$ , where  $\xi$  is a positive rescaling coefficient introduced to adjust the scale difference between point-wise distance and time. The bottleneck distance  $d_{B, \xi}^{(3)}(Dg_1^{(3)}, Dg_2^{(3)})$  between  $Dg_1^{(3)}$  and  $Dg_2^{(3)}$  is defined as the infimum of the longest matched relative infinity-norm distance over all matchings,  $\psi$ :

$$d_{B, \xi}^{(3)}(Dg_1^{(3)}, Dg_2^{(3)}) = \inf_{\psi} \max_{(\mathbf{p}, \mathbf{q}) \in \psi} d_\xi^{(\infty)}(\mathbf{p}, \mathbf{q}). \quad (\text{S4})$$

We prove the next theorem, which leads to the Eq. (2) proposed in the main text.

**Theorem S1** *Consider two time series  $x(t)$  and  $y(t)$  with the same length. Consider  $\tau$  in a pre-defined set  $\mathcal{T} = \{\tau_1, \tau_2, \dots, \tau_K\}$ , where  $\tau_1 < \tau_2 < \dots < \tau_K$  (with  $K$  denoting the set's size) are sampled from the domain of  $\tau$ . Let  $Dg_{(m)}^{(3)}(x)$  and  $Dg_{(m)}^{(3)}(y)$  be 3-dimensional persistence diagrams of  $x(t)$  and  $y(t)$ , respectively, calculated at the embedding dimension  $m$ . Given the positive rescaling coefficient  $\xi$ , we have the following stability properties of 3-dimensional persistence diagrams,*

$$d_{B, \xi}^{(3)}(Dg_{(m)}^{(3)}(x), Dg_{(m)}^{(3)}(y)) \leq 2 \max_{\tau \in \mathcal{T}} d_H(X_{(m)}^\tau, Y_{(m)}^\tau) \leq 2\sqrt{m} \max_t |x(t) - y(t)|, \quad (\text{S5})$$

where  $X_{(m)}^\tau$  and  $Y_{(m)}^\tau$  are the embedded points of  $x(t)$  and  $y(t)$ , respectively, in an embedding space with dimension  $m$  and time delay  $\tau$ .

*Proof.* For each  $\tau \in \mathcal{T}$ , we denote the 2-dimensional persistence diagrams calculated from embedded points  $X_{(m)}^\tau$  and  $Y_{(m)}^\tau$  as  $Dg^{(2)}(X_{(m)}^\tau)$  and  $Dg^{(2)}(Y_{(m)}^\tau)$ , respectively. Let  $\Gamma_\tau$  be the set of matchings defined in Eq. (S1) between two 2-dimensional persistence diagrams  $Dg^{(2)}(X_{(m)}^\tau)$  and  $Dg^{(2)}(Y_{(m)}^\tau)$ . For each collection  $\Lambda = \{\gamma_1, \gamma_2, \dots, \gamma_K \mid \gamma_i \in \Gamma_{\tau_i}, i = 1, 2, \dots, K\}$ , we construct a matching  $\psi$  between two 3-dimensional persistence diagrams  $Dg_{(m)}^{(3)}(x)$  and  $Dg_{(m)}^{(3)}(y)$ , such that, for each  $(\mathbf{p}, \mathbf{q}) \in \psi$ , then  $\mathbf{p} = (b_1, d_1, \tau)$ ,  $\mathbf{q} = (b_2, d_2, \tau)$ , and  $(\mathbf{p}_\gamma, \mathbf{q}_\gamma) \in \gamma$ , where  $\mathbf{p}_\gamma = (b_1, d_1)$ ,  $\mathbf{q}_\gamma = (b_2, d_2)$ , and  $\gamma \in \Lambda \cap \Gamma_\tau$ . Let  $\Gamma$  be the set of all matchings  $\psi$  constructed this way. From the definition of bottleneck distance, we have the following inequality:

$$d_{B, \xi}^{(3)}(Dg_{(m)}^{(3)}(x), Dg_{(m)}^{(3)}(y)) \leq \inf_{\psi \in \Gamma} \max_{(\mathbf{p}, \mathbf{q}) \in \psi} d_\xi^{(\infty)}(\mathbf{p}, \mathbf{q}). \quad (\text{S6})$$

For  $(\mathbf{p}, \mathbf{q}) \in \psi$ , we have

$$d_\xi^{(\infty)}(\mathbf{p}, \mathbf{q}) = \max\{|b_1 - b_2|, |d_1 - d_2|, \xi|\tau - \tau|\} \quad (\text{S7})$$

$$= \max\{|b_1 - b_2|, |d_1 - d_2|\} = \|\mathbf{p}_\gamma - \mathbf{q}_\gamma\|_\infty, \quad (\text{S8})$$



and Eq. (S6) becomes

$$d_{B,\xi}^{(3)}(Dg_{(m)}^{(3)}(x), Dg_{(m)}^{(3)}(y)) \leq \max_{\tau \in \mathcal{T}} \inf_{\gamma \in \Gamma_\tau} \max_{(\mathbf{p}_\gamma, \mathbf{q}_\gamma) \in \gamma} \|\mathbf{p}_\gamma - \mathbf{q}_\gamma\|_\infty \quad (\text{S9})$$

$$= \max_{\tau \in \mathcal{T}} d_B^{(2)}(Dg^{(2)}(X_{(m)}^\tau), Dg^{(2)}(Y_{(m)}^\tau)). \quad (\text{S10})$$

From Eq. (S10) and Proposition S1, we have the following result:

$$d_{B,\xi}^{(3)}(Dg_{(m)}^{(3)}(x), Dg_{(m)}^{(3)}(y)) \leq \max_{\tau \in \mathcal{T}} d_B^{(2)}(Dg^{(2)}(X_{(m)}^\tau), Dg^{(2)}(Y_{(m)}^\tau)) \leq 2 \max_{\tau \in \mathcal{T}} d_H(X_{(m)}^\tau, Y_{(m)}^\tau). \quad (\text{S11})$$

Next, we prove the second part of the inequality. We consider  $\mathcal{X}_{(m)}^\tau(t_0) = (x(t_0), x(t_0 - \tau), \dots, x(t_0 - (m-1)\tau)) \in X_{(m)}^\tau$  and  $\mathcal{Y}_{(m)}^\tau(t_0) = (y(t_0), y(t_0 - \tau), \dots, y(t_0 - (m-1)\tau)) \in Y_{(m)}^\tau$  at each time point  $t_0$ . From the definition of Euclidean distance, we have the following result:

$$d(\mathcal{X}_{(m)}^\tau(t_0), \mathcal{Y}_{(m)}^\tau(t_0)) = \sqrt{\sum_{i=0}^{m-1} [x(t_0 + i\tau) - y(t_0 + i\tau)]^2} \leq \sqrt{m} \|x(t) - y(t)\|_\infty. \quad (\text{S12})$$

From Eq. (S12) and the definition of Hausdorff distance, we have the following inequality:

$$d_H(X_{(m)}^\tau, Y_{(m)}^\tau) = \max \left\{ \max_{t_1} \min_{t_2} d(\mathcal{X}_{(m)}^\tau(t_1), \mathcal{Y}_{(m)}^\tau(t_2)), \max_{t_2} \min_{t_1} d(\mathcal{X}_{(m)}^\tau(t_1), \mathcal{Y}_{(m)}^\tau(t_2)) \right\} \quad (\text{S13})$$

$$\leq \max \left\{ \max_{t_1} d(\mathcal{X}_{(m)}^\tau(t_1), \mathcal{Y}_{(m)}^\tau(t_1)), \max_{t_2} d(\mathcal{X}_{(m)}^\tau(t_2), \mathcal{Y}_{(m)}^\tau(t_2)) \right\} \quad (\text{S14})$$

$$\leq \sqrt{m} \|x(t) - y(t)\|_\infty. \quad (\text{S15})$$

The second part of the theorem is obtained by taking the maximum of Eq. (S15) over  $\tau \in \mathcal{T}$  and applying it to Eq. (S11).

When we identify  $y(t)$  as the perturbed data obtained by adding noise to  $x(t)$ , Theorem S1 shows that the bottleneck distance between  $Dg_{(m)}^{(3)}(x)$  and  $Dg_{(m)}^{(3)}(y)$  is bounded from above by the magnitude of the noise.

### 3 Kernel for the 3-dimensional persistence diagrams

#### 3.1 Proof for the positive-definite property of the kernel

We prove that the proposed kernel for the 3-dimensional persistence diagrams in the main text is positive-definite. We prove for the case when the positive rescaling coefficient  $\xi = 1$ . The proof is straightforward for other positive values of  $\xi$ . Please refer to [3] for the proof for the kernel of the 2-dimensional persistence diagrams.

For each parameter  $\sigma$  and a 3-dimensional persistence diagram  $Dg^{(3)}$ , we define the following feature mapping  $\Phi_\sigma : \mathcal{D}^{(3)} \rightarrow L^2(\Omega)$ , where  $\mathcal{D}^{(3)}$  is the space of 3-dimensional persistence diagrams,  $\Omega = \{\mathbf{x} = (x_1, x_2, x_3) \mid x_1, x_2, x_3 \in \mathbb{R}, x_1 \leq x_2\}$  and  $L^2(\Omega)$  is the Hilbert space of square-integrable  $L^2$ -functions defined on the domain  $\Omega$ :

$$\Phi_{\sigma,\xi}(Dg^{(3)})(\mathbf{x}) = \frac{1}{\sqrt{\kappa}} \sum_{\mathbf{p} \in Dg^{(3)}} e^{-\frac{\|\mathbf{x} - \mathbf{p}\|^2}{\sigma^2}} - e^{-\frac{\|\mathbf{x} - \bar{\mathbf{p}}\|^2}{\sigma^2}}, \quad (\text{S16})$$

where  $\bar{\mathbf{p}}$  is a symmetric point of  $\mathbf{p}$  with respect to diagonal plane  $\mathcal{W}^{(3)}$  on  $\mathbb{R}^3$  and  $\kappa$  is a positive value depending on  $\sigma$ , which we will show later.

We show that the kernel defined in the main text is the inner product of  $\Phi_\sigma$  on  $L^2(\Omega)$  as

$$k_{\sigma,\xi}(Dg_1^{(3)}, Dg_2^{(3)}) = \langle \Phi_{\sigma,\xi}(Dg_1^{(3)}), \Phi_{\sigma,\xi}(Dg_2^{(3)}) \rangle_{L^2(\Omega)} \quad (\text{S17})$$

$$= \int_{\Omega} \Phi_{\sigma,\xi}(Dg_1^{(3)})(\mathbf{x}) \Phi_{\sigma,\xi}(Dg_2^{(3)})(\mathbf{x}) d\mathbf{x}. \quad (\text{S18})$$

We extend the domain of function  $\Phi_{\sigma,\xi}(Dg^{(3)})(\mathbf{x})$  from  $\Omega$  to  $\mathbb{R}^3$  to obtain a function that is symmetric with respect to the diagonal plane  $\mathcal{W}^{(3)}$  (because  $\|\mathbf{x} - \mathbf{p}\| = \|\bar{\mathbf{x}} - \bar{\mathbf{p}}\|$  and  $\|\mathbf{x} - \bar{\mathbf{p}}\| = \|\bar{\mathbf{x}} - \mathbf{p}\|$ ). Then we have

$$\int_{\Omega^{(3)}} \Phi_{\sigma,\xi}(Dg_1^{(3)})(\mathbf{x}) \Phi_{\sigma,\xi}(Dg_2^{(3)})(\mathbf{x}) d\mathbf{x} = \frac{1}{2} \int_{\mathbb{R}^3} \Phi_{\sigma,\xi}(Dg_1^{(3)})(\mathbf{x}) \Phi_{\sigma,\xi}(Dg_2^{(3)})(\mathbf{x}) d\mathbf{x} \quad (\text{S19})$$

$$= \frac{1}{2\kappa} \sum_{\mathbf{p} \in Dg_1^{(3)}} \sum_{\mathbf{q} \in Dg_2^{(3)}} [A(\mathbf{p}, \mathbf{q}) + A(\bar{\mathbf{p}}, \bar{\mathbf{q}}) - A(\bar{\mathbf{p}}, \mathbf{q}) - A(\mathbf{p}, \bar{\mathbf{q}})], \quad (\text{S20})$$

where  $A(\mathbf{c}, \mathbf{d})$  is defined as

$$A(\mathbf{c}, \mathbf{d}) = \int_{\mathbb{R}^3} e^{-\frac{\|\mathbf{x} - \mathbf{c}\|^2 + \|\mathbf{x} - \mathbf{d}\|^2}{\sigma^2}} d\mathbf{x} = \int_{\mathbb{R}^3} e^{-\frac{\|\mathbf{x} - (\mathbf{c} - \mathbf{d})\|^2 + \|\mathbf{x}\|^2}{\sigma^2}} d\mathbf{x} = \frac{\sigma^3(2\pi)^{3/2}}{8} e^{-\frac{\|\mathbf{c} - \mathbf{d}\|^2}{2\sigma^2}}. \quad (\text{S21})$$

Here,  $\mathbf{c}, \mathbf{d} \in \mathbb{R}^3$ . From Eqs. (S20) and (S21) we have

$$k_{\sigma, \xi}(Dg_1^{(3)}, Dg_2^{(3)}) = \frac{\sigma^3(2\pi)^{3/2}}{16\kappa} \sum_{\mathbf{p} \in Dg_1^{(3)}} \sum_{\mathbf{q} \in Dg_2^{(3)}} \left( e^{-\frac{\|\mathbf{p} - \mathbf{q}\|^2}{2\sigma^2}} + e^{-\frac{\|\bar{\mathbf{p}} - \bar{\mathbf{q}}\|^2}{2\sigma^2}} - e^{-\frac{\|\bar{\mathbf{p}} - \mathbf{q}\|^2}{2\sigma^2}} - e^{-\frac{\|\mathbf{p} - \bar{\mathbf{q}}\|^2}{2\sigma^2}} \right). \quad (\text{S22})$$

Since  $\|\mathbf{p} - \mathbf{q}\|^2 = \|\bar{\mathbf{p}} - \bar{\mathbf{q}}\|^2$ ,  $\|\bar{\mathbf{p}} - \mathbf{q}\|^2 = \|\mathbf{p} - \bar{\mathbf{q}}\|^2$ , we have the closed form of the kernel as shown in the main text:

$$k_{\sigma, \xi}(Dg_1^{(3)}, Dg_2^{(3)}) = \frac{1}{\sigma\sqrt{2\pi}} \sum_{\mathbf{p} \in Dg_1^{(3)}} \sum_{\mathbf{q} \in Dg_2^{(3)}} e^{-\frac{\|\mathbf{p} - \mathbf{q}\|^2}{2\sigma^2}} - e^{-\frac{\|\mathbf{p} - \bar{\mathbf{q}}\|^2}{2\sigma^2}}, \quad (\text{S23})$$

where  $\kappa = \frac{\pi^2\sigma^4}{2}$ .

The kernel is positive-definite due to the inner-product nature of the feature mapping. Consider the 3-dimensional persistence diagrams  $Dg_1^{(3)}, Dg_2^{(3)}, \dots, Dg_N^{(3)}$  of the  $l$ -dimensional holes that are needed to compute the kernel. The Gram matrix for these diagrams is defined as  $\mathbf{K}_{N \times N}^{(l)} = [k_{ij}]$ , whose element  $k_{ij}$  is  $k_{ij} = k_{\sigma, \xi}(Dg_i^{(3)}, Dg_j^{(3)})$  with  $i = 1, 2, \dots, N$  and  $j = 1, 2, \dots, N$ .

### 3.2 Selecting parameters for the kernel

We denote the sets of time-delay values used to compute  $Dg_1^{(3)}$  and  $Dg_2^{(3)}$  as  $\mathcal{T}_1$  and  $\mathcal{T}_2$ , respectively. For each  $\tau$ , we use the notation  $Dg_{1,(\tau)}^{(2)} = \{\mathbf{p}_\tau = (b, d) \mid \mathbf{p} = (b, d, \tau) \in Dg_1^{(3)}\}$ , with  $Dg_{2,(\tau)}^{(2)}$  having a similar meaning. Then, Eq. (S23) becomes

$$k_{\sigma, \xi}(Dg_1^{(3)}, Dg_2^{(3)}) = \frac{1}{\sigma\sqrt{2\pi}} \sum_{\tau_1 \in \mathcal{T}_1} \sum_{\tau_2 \in \mathcal{T}_2} e^{-\frac{\xi^2|\tau_1 - \tau_2|^2}{2\sigma^2}} \sum_{\substack{\mathbf{p}^{(2)} \in Dg_{1,(\tau_1)}^{(2)} \\ \mathbf{q}^{(2)} \in Dg_{2,(\tau_2)}^{(2)}}} e^{-\frac{\|\mathbf{p}^{(2)} - \mathbf{q}^{(2)}\|^2}{2\sigma^2}} - e^{-\frac{\|\mathbf{p}^{(2)} - \bar{\mathbf{q}}^{(2)}\|^2}{2\sigma^2}}, \quad (\text{S24})$$

where  $\bar{\mathbf{q}}^{(2)}$  is a symmetric point of  $\mathbf{q}^{(2)}$  with respect to the diagonal line  $\mathcal{W}^{(2)}$  on  $\mathbb{R}^2$ .

In time-series classification experiments, we compute the kernel by taking time-delay values as discrete values with sampling interval 1 and set the rescale coefficient to  $\xi = \sigma$ . The selection of kernel bandwidth  $\sigma$  can be chosen by cross-validation; however, as proposed in [4], we present here a heuristic way to select  $\sigma$ . Consider the 3-dimensional persistence diagrams  $Dg_1^{(3)}, Dg_2^{(3)}, \dots, Dg_N^{(3)}$  that are required to compute the kernel. We denote  $\sigma_s^2 = \text{median}\{(b_i - b_j)^2 + (d_i - d_j)^2 \mid (b_i, d_i, \tau_i), (b_j, d_j, \tau_j) \in Dg_s^{(3)}\}$  with  $s = 1, 2, \dots, N$ . In our time-series classification experiments,  $\sigma$  is set as  $\sigma^2 = \frac{1}{2} \text{median}\{\sigma_s^2 \mid s = 1, \dots, N\}$ , such that  $2\sigma^2$  takes values close to many  $(b_i - b_j)^2 + (d_i - d_j)^2$  values.

### 3.3 Using kernels with holes of multiple dimensions

For all  $l$ -dimensional holes, we obtain the persistence diagrams and compute their kernels as  $k_{\sigma_l, \xi_l}$ , where  $\sigma_l$  is the bandwidth of this kernel and  $\xi_l$  is the positive rescaling coefficient corresponding with  $l$ -dimensional holes. To use persistence diagrams for different dimensions of holes, we can combine the kernels at various dimensions through linear combinations. In our time-series classification experiments, we only consider the topological features of 0-dimensional holes (connected components or clusters) and 1-dimensional holes (loops). Thus, the combined Gram matrix of  $N$  data can be defined as

$$\mathbf{K}_{N \times N} = \alpha_0 \mathbf{K}_{N \times N}^{(0)} + \alpha_1 \mathbf{K}_{N \times N}^{(1)}, \quad (\text{S25})$$

where  $0 \leq \alpha_0, \alpha_1 \leq 1$ ,  $\alpha_0 + \alpha_1 = 1$ , and  $\mathbf{K}_{N \times N}^{(0)}$  and  $\mathbf{K}_{N \times N}^{(1)}$  are the Gram matrices of  $N$  persistence diagrams at the 0-dimensional and 1-dimensional holes, respectively. In our time-series classification experiments, we choose  $\alpha_0$  from  $\{0, 0.0001, 0.0002, 0.0005, 0.001, 0.002, 0.005, 0.01, 0.02, 0.05, 0.1, 0.2, 0.5, 1.0\}$  by cross-validation.

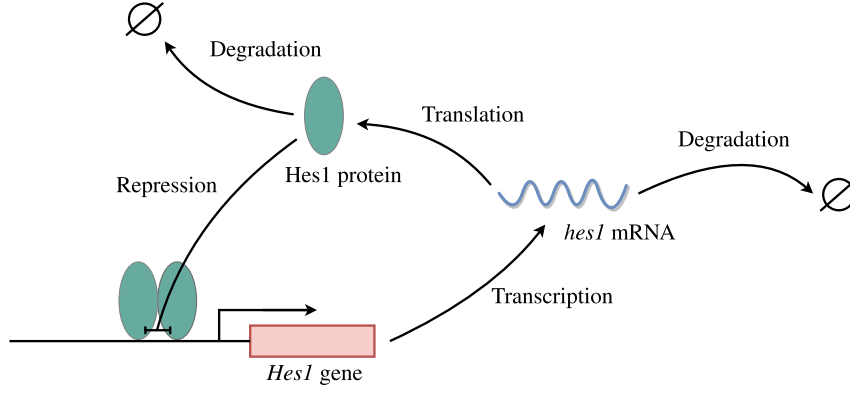


Figure S3: Schematic of the Hes1 regulatory model. mRNA molecules are produced by the transcription of DNA. The production of Hes1 protein occurs by translation of *hes1* mRNA with delay time  $\zeta$ . The Hes1 protein represses its own expression by directly binding to its promoter as negative feedback.

## 4 Synthetic Hes1 model data

We generate data from Hes1 regulatory model, which is a stochastic model of a *Hes1* genetic oscillator which consists of negative auto-regulation with delay [6, 7]. The network topology of the model is illustrated in Fig. S3. The model describes the concentrations and interactions of two types of particles: *hes1* mRNA molecules, denoted by  $M$ , and Hes1 protein molecules, denoted by  $P$ . The stochastic dynamics are defined by the following four reactions:



The degradations of mRNA and protein are described in reactions (S26) and (S27), respectively, where the rates of these degradation are  $\mu_m$  and  $\mu_p$ , respectively. mRNA molecules are translated into protein via reaction (S28) by the translation-rate parameter  $\beta_p$ . The final reaction, (S29) with a double arrow describes the transcription process for producing mRNA which is accompanied by time delay. The rate of *hes1* mRNA production depends on the concentration of Hes1 protein molecules through a negative-feedback mechanism, as described by the function  $g(n_p) = \beta_m \left[ 1 + [n_p / (P_0 \Theta)]^h \right]^{-1}$ , where  $n_p$  is the number of protein molecules in the system,  $\beta_m$ ,  $P_0$ , and  $h$  are constants, and  $\Theta$  is the size of the system. This transcription process is associated with a time delay  $\zeta$  drawn from a distribution  $K(\zeta)$ ; that is, the protein concentration at time  $t - \zeta$  only affects the production of mRNA at time  $t$ . The data is simulated using the delayed version of the Gillespie algorithm [8, 9]. The simulation program is provided in [5] and we generate data from 1,000 cells in both oscillatory and non-oscillatory parameter regimes [7, 10]. In the simulations, the protein levels were measured every  $\nu$  ( $\nu = 32, 16, 8, 4, 2, 1$ ) min for 4,096 mins. The measurements start at  $t = 5,000$ min for the system to equilibrate. We add the noise with a variance of 10% of a signal at each time point to show the robustness of the method.

To confirm that the parameter regimes used in the simulation are oscillatory or non-oscillatory, we apply the Fourier transform to the generated time-series data at the measured interval  $\nu = 1$ min. Although the power spectrum cannot be used to distinguish two regimes with individual time series, the average power spectrum of 1,000 data points in each parameter regime shows clear oscillatory or non-oscillatory behavior (Fig. S4). In the oscillatory regime, there is a clear peak at a frequency of  $0.5 \text{ hours}^{-1}$ , whereas the average power spectrum in the non-oscillatory regime shows no peak.

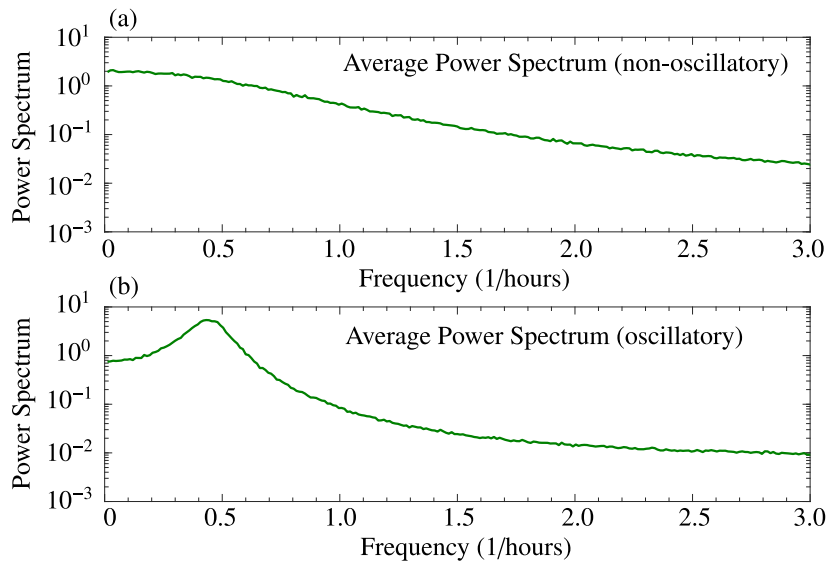


Figure S4: Average power spectra of the protein concentrations calculated from Gillespie simulation of 1,000 independent non-oscillating data points (a) and 1,000 oscillating data points (b). The measurements start at  $t = 5,000\text{min}$  for the system to equilibrate. Parameters for (a) are  $P_0 = 300, h = 1, \zeta = 0, \beta_m = \beta_p = 1, \mu_m = \mu_p = 0.07, \Theta = 20$ , and for (b) are  $P_0 = 100, h = 3, \zeta = 18, \beta_m = \beta_p = 1, \mu_m = \mu_p = 0.03, \Theta = 20$ . The time series are generated with measurements every 1 min over a period of  $t = 9,096\text{min}$ .

## 5 Description of real electrocardiogram data

We evaluate the performance of delay-variant method in classifying different heartbeat-signal patterns from six real electrocardiogram (ECG) datasets in [12], namely, ECG200 (separate normal and myocardial infarction heartbeats, for 200 time series of length 96), ECG5000 (separate five levels of congestive heart failure, for 5000 time series of length 140), ECGFiveDays (separate records from two different days for the same patient, for 884 time series of length 136), TwoLeadECG (separate records from two different leads, for 1162 time series of length 82), Non-InvasiveFetalECGThorax1 and Non-InvasiveFetalECGThorax2 (separate records from the left and right thorax with expert labeling into 42 classes of non-invasive fetal ECG, for 3765 time series of length 750 in each dataset). For this purpose, we employ the train-test split provided in [12].

## 6 The projection of features from the kernel space

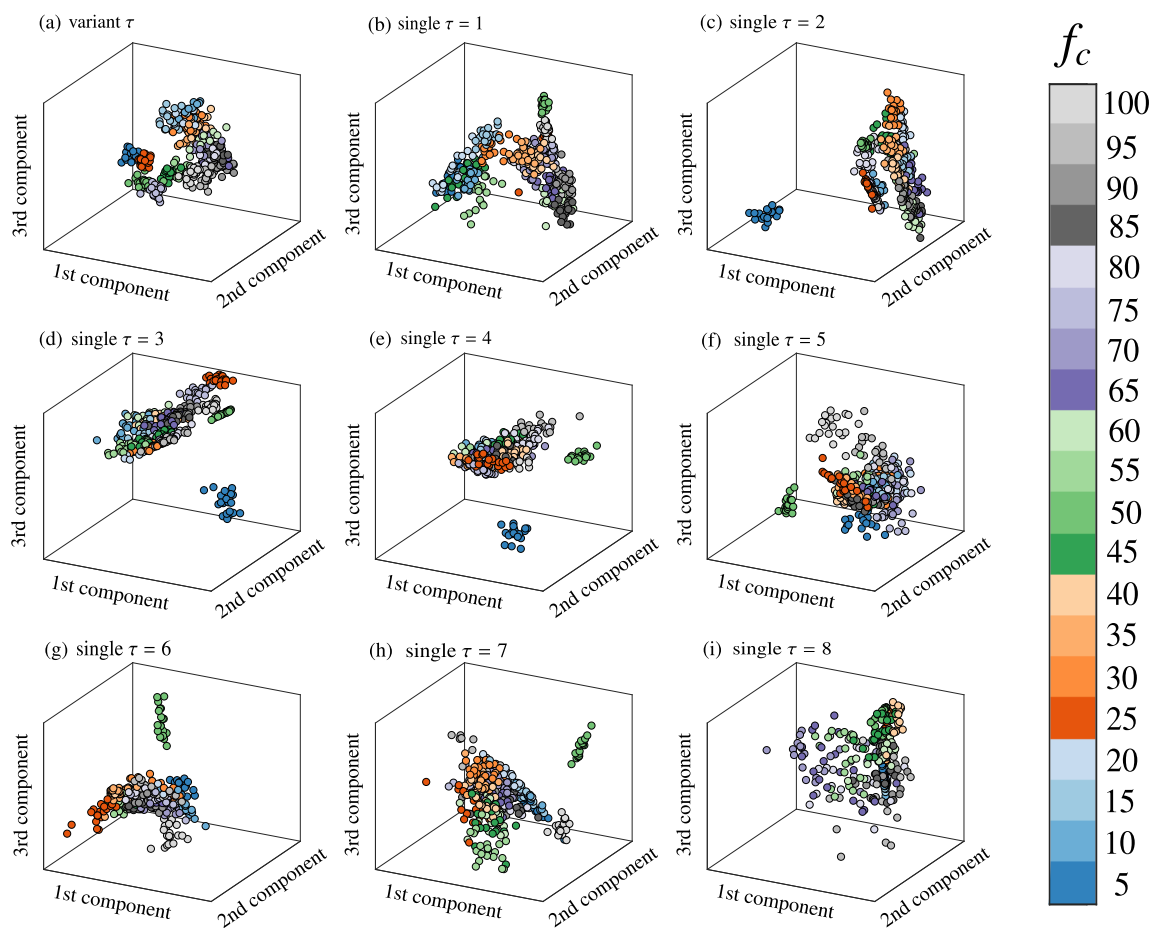


Figure S5: The projection of features for synthetic frequency modulated time series data from the kernel space to the 3-dimensional principal components for (a) delay-variant method at an effective embedding dimension  $M = 60$  with  $K = 20$  time-delay values  $\tau_1 = 1, \dots, \tau_{20} = 20$ , and (b)(c)(d)(e)(f)(g)(h)(i) single-delay method at an effective embedding dimension  $M = 60$  and a single  $\tau$  for (b)  $\tau = 1$ , (c)  $\tau = 2$ , (d)  $\tau = 3$ , (e)  $\tau = 4$ , (f)  $\tau = 5$ , (g)  $\tau = 6$ , (h)  $\tau = 7$ , and (i)  $\tau = 8$ . Different colors represent data generated from different values of the carrier frequency,  $f_c$ .



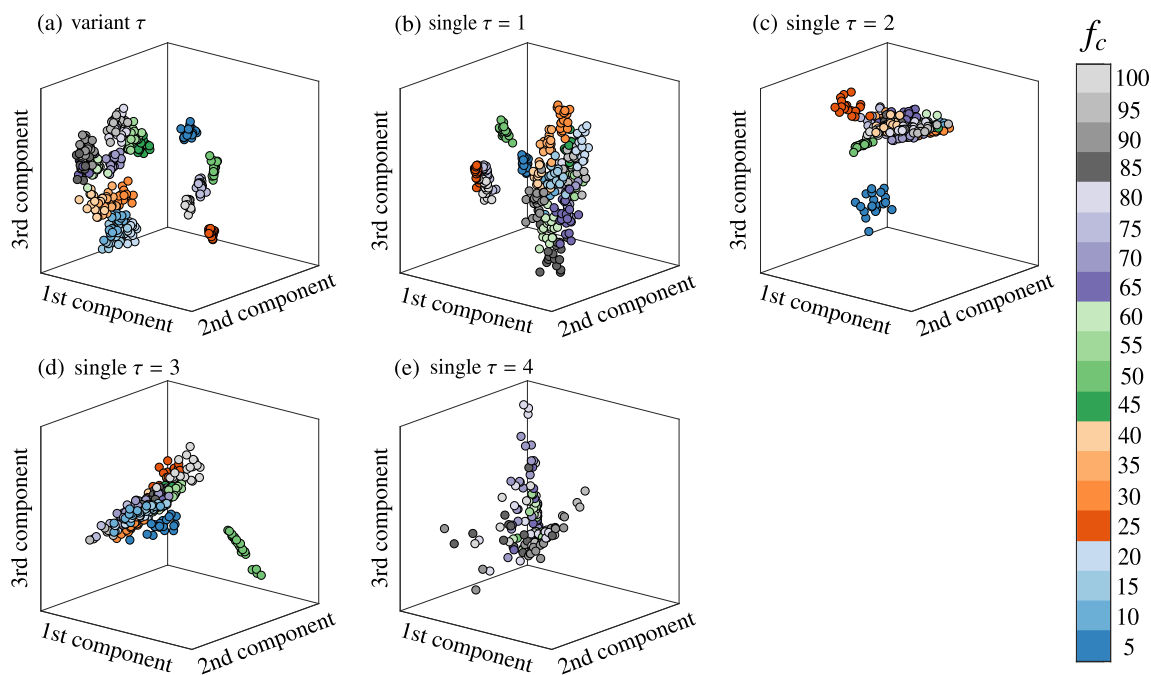


Figure S6: The projection of features for synthetic frequency modulated time series data from the kernel space to the 3-dimensional principal components for (a) delay-variant method at an effective embedding dimension  $M = 120$  with  $K = 20$  time-delay values  $\tau_1 = 1, \dots, \tau_{20} = 20$ , and (b)(c)(d)(e) single-delay method at an effective embedding dimension  $M = 120$  and a single  $\tau$  for (b)  $\tau = 1$ , (c)  $\tau = 2$ , (d)  $\tau = 3$ , (e)  $\tau = 4$ . Different colors represent data generated from different values of the carrier frequency,  $f_c$ .

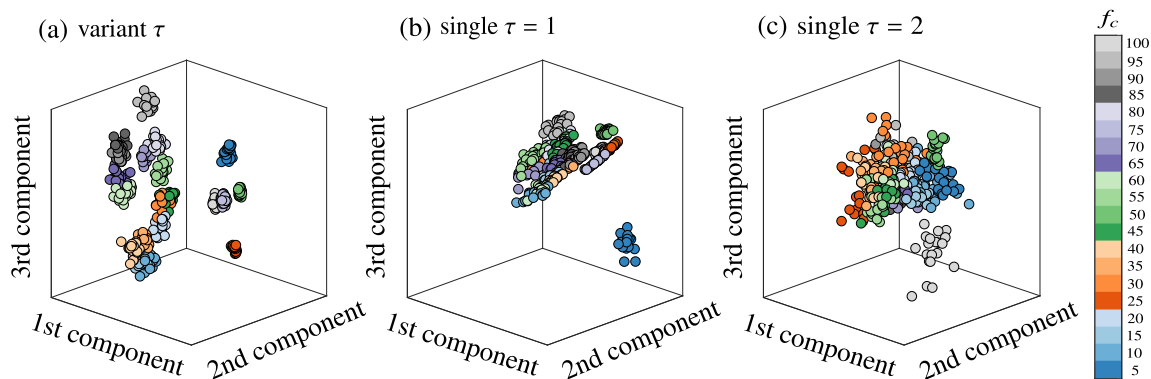


Figure S7: The projection of features for synthetic frequency modulated time series data from the kernel space to the 3-dimensional principal components for (a) delay-variant method at an effective embedding dimension  $M = 180$  with  $K = 20$  time-delay values  $\tau_1 = 1, \dots, \tau_{20} = 20$ , and (b)(c) single-delay method at an effective embedding dimension  $M = 180$  and a single  $\tau$  for (b)  $\tau = 1$ , (c)  $\tau = 2$ . Different colors represent data generated from different values of the carrier frequency,  $f_c$ .

## References

- [1] H. Edelsbrunner, J. Harer. Computational topology. An introduction. Amer. Math. Soc., 2010.
- [2] F. Chazal, V. de Silva and S. Oudot. Persistence stability for geometric complexes. *Geometriae Dedicata*, 173(1):193-214, 2014.
- [3] J. Reininghaus, S. Huber, U. Bauer and R. Kwitt. A stable multi-scale kernel for topological machine learning. *2015 IEEE Conf. Computer Vision and Pattern Recognition (CVPR)*, 2015.

- [4] A. Gretton, K. Fukumizu, C. H. Teo, L. Song, B. Schölkopf and A. J. Smola. A kernel statistical test of independence. *Advances in Neural Information Processing Systems 20*, 2008.
- [5] N. E. Phillips, C. Manning, N. Papalopulu, and M. Rattay. Identifying stochastic oscillations in single-cell live imaging time series using Gaussian processes. *PLOS Comp. Biol.*, 13(5), 2017.
- [6] N. A. Monk. Oscillatory expression of Hes1, p53, and NF- $\kappa$ B driven by transcriptional time delays. *Curr. Biol.*, 13(16):1409–1413, 2003.
- [7] T. Galla. Intrinsic fluctuations in stochastic delay systems: Theoretical description and application to a simple model of gene regulation. *Phys. Rev. E*, 80(2):021909, 2009.
- [8] D. T. Gillespie. Exact stochastic simulation of coupled chemical reactions. *J. Phys. Chem.*, 81(25):2340–2361, 1977.
- [9] D. F. Anderson. A modified next reaction method for simulating chemical systems with time dependent propensities and delays. *J. Phys. Chem.*, 127(21):214107, 2007.
- [10] T. Brett and T. Galla. Stochastic processes with distributed delays: chemical Langevin equation and linear-noise approximation. *Phys. Rev. Lett.*, 110(25):250601, 2013.
- [11] A. M. Fraser and H. L. Swinney. Independent coordinates for strange attractors from mutual information. *Phys. Rev. A*, 33(2):1134–1140, 1986.
- [12] A. Bagnall, J. Lines, W. Vickers, and E. Keogh. The UFA & UCR Time Series Classification Repository. [www.timeseriesclassification.com](http://www.timeseriesclassification.com).